Journal of Materials Chemistry A

ROYAL SOCIETY OF CHEMISTRY

PAPER

View Article Online
View Journal | View Issue

Cite this: J. Mater. Chem. A, 2024, 12, 1530

A ZnO&GeSe composite electron transport layer for organic solar cells†

Jingyu Tan, Hongye Li, Yapeng Sun, Guanliang Li, Yujun Zhao and Huangzhong Yu *

In organic solar cells (OSCs), ZnO is a widely used electron transport layer (ETL), but various vacancy defects on the surface of ZnO crystals form massive trap-assisted recombination centers, which hinders electron transmission in OSCs. In this paper, a ZnO&GeSe composite is constructed by modifying ZnO with two-dimensional (2D) GeSe, and it is used for the first time as a novel ETL in OSCs, which reduces the defect density on the ZnO surface and improves the electron extraction efficiency in OSCs. The results of first-principles calculations show that GeSe can deposit additional electrons on the surface of ZnO, which stabilizes the ZnO polar surface and reduces the formation of spontaneous defects on the ZnO polar surface. The electric dipole moment formed at the interface also promotes electron transport in OSCs. The power conversion efficiency (PCE) of OSCs based on PBDB-T:ITIC and PM6:Y6 active layers increases from 10.06% and 15.20% to 11.68% and 17.51%, respectively. Meanwhile, the OSC with the ZnO&GeSe composite ETL possesses good stability compared to the device with the pure ZnO ETL. This study shows that 2D GeSe has a good application prospect as a charge transport layer, and provides an idea for the defect modification of ZnO and other semiconductor crystals by 2D materials.

Received 28th September 2023
Accepted 28th November 2023

DOI: 10.1039/d3ta05900f

rsc.li/materials-a

Introduction

As a kind of renewable energy source with light weight and large-scale manufacturing by a roll-to-roll printing process, organic solar cells (OSCs) have attracted the attention of many scientists in today's world where the proportion of electrical energy is increasing.[1–7] In order to seek high power conversion efficiency (PCE) and good stability of OSCs, researchers have conducted a lot of research on organic light absorption materials, interface layer materials and electrode materials.[3–5] In the latest research, the PCE of single junction OSCs has exceeded 19%.[6,7] Although the development of new organic photovoltaic materials and the optimization of the active layer are dominant in the research on OSCs, the development and improvement of the interface layer are also important. Since the interface transport layer, including the electron transport layer (ETL) and hole transport layer (HTL), plays a key role in the transport of carriers, it greatly affects the collection efficiency of photogenerated charges on the electrode and ultimately feeds back to the device performance. ZnO is a widely used ETL in inverted OSCs.[8,9] However, in the practical application process, various defects and a large number of dangling bonds on the surface of the ZnO crystal form charge recombination centers, resulting in the recombination of photogenerated carriers in ZnO and hindering charge transfer.[10] The energy level mismatch between the conduction band of ZnO and the lowest unoccupied molecular orbital (LUMO) energy of the active layer material, and the interface incompatibility caused by the large hydrophilic–hydrophobic gap between ZnO and the active layer also restrict the further improvement of the performance of the device with ZnO as the ETL. These factors seriously affect the efficiency of inverted OSCs, making the efficiency of inverted OSCs significantly lower than that of formal structure OSCs. Therefore, how to improve the electrical properties of ZnO and enhance its carrier transport and collection capabilities is a very valuable research topic.

Previous studies on ZnO crystals have mentioned that the surface of ZnO is unstable because the oppositely charged particles of Zn and O establish a net dipole field accumulating along the z direction on the surface of ZnO.[11,12] The deposition of additional electrons on the surface of Zn can offset the dipole field, which improves the stability of the ZnO surface and reduces the formation probability of defect vacancies.[13] Among the numerous research methods to improve the performance of ZnO, a promising strategy is to modify the surface of ZnO with targeted materials. For inverted OSCs, the ETL located at the bottom of the active layer not only selectively transports electrons and blocks holes, but also affects the crystalline morphology of the active layer. Therefore, the selection of ZnO surface modification layer materials must be cautiously done.

School of Physics and Optoelectronics, South China University of Technology, Guangzhou 510640, Guangdong, China. E-mail: hzhyu@scut.edu.cn

† Electronic supplementary information (ESI) available. See DOI: https://doi.org/10.1039/d3ta05900f

Some research groups have used 2D materials to modify semiconductor crystals (ZnO, SnO_2, *etc.*) and construct composite electron transport layers. For example, Lin *et al.* reported that the solution-exfoliated 2D few-layer black phosphorus (BP) material was spin-coated on ZnO as an efficient composite ETL in OSCs, which significantly improved the PCE of the device.[14] Wang *et al.* proposed a composite ETL of amorphous WO_3 and SnO_2, which effectively blocked the transport of holes and improved the extraction efficiency of electrons.[15] Chen *et al.* prepared a SnO_2&Bi_2O_2Se composite ETL by using high carrier mobility 2D Bi_2O_2Se, which effectively reduced the trap recombination of carriers at the interface.[16] However, most studies only explain the changes in the properties of semiconductor crystals from experimental phenomena, but the physical mechanism of 2D materials reducing the defect density of semiconductor crystals has not been deeply explored. Using functional groups with special functions to fill the defect vacancies of ZnO crystals is a widely used theoretical explanation in the study of organic molecule modified ZnO crystals.[17,18] However, it is difficult to explain the phenomenon that 2D material modification reduces defect vacancies in ZnO crystals.

In this work, we use a 2D germanium selenide (GeSe) modified ZnO crystal to construct a ZnO&GeSe composite, and utilize it as novel ETL in OSCs; the device structure is shown in Fig. 1a. Furthermore, we use first-principles calculations to find that the modification of GeSe can promote electron transport efficiency of ZnO at the micro-level, and reveal the reasons for the stability improvement of the ZnO polar surface, and further study the effect of 2D GeSe on the formation energy of ZnO surface defects. More importantly, we use XPS, XRD, PL and other experimental characterizations to verify the correctness and rationality of the theoretical calculation from the macro-level. The actual situation of charge transfer between ZnO and GeSe and the change of ZnO crystal defect density are analyzed, which proves the reliability of the theoretical research conclusion.

Results and discussion

GeSe is a kind of IV–VI semiconductor, which is composed of covalently coordinated Ge–Se double-layer atoms to form the orthorhombic crystal structure (Fig. 1b) of *Pnma* 62 space group.[19] GeSe crystallizes into a layered structure, and the van der Waals (vdW) force between the atomic layers makes that bulk GeSe exfoliate into few layers or even single-layered nanosheets by shear force. The theoretical values of electron mobility and hole mobility of 2D GeSe are 10^3 cm^2 V^{-1} s^{-1} and 10^2 cm^2 V^{-1} s^{-1} respectively, which provides a basis for achieving efficient carrier transport and collection.[20,21] Transmission electron microscopy (TEM) is used to measure the size of 2D GeSe. As shown in Fig. 2a and b, the size of large-area few-layer GeSe nanosheets is mostly concentrated between 150 and 200 nm, and some GeSe nanosheets with a size of about 20 nm are also detected. Large-sized GeSe nanosheets can form an ETL on ZnO crystals, inhibit the dissociation of Zn and O atoms on the surface, and reduce the number of surface defect vacancies in ZnO crystals. And the small size of GeSe nanosheets can fill the crystal plane gap between ZnO crystals and make the surface of ZnO smoother, thereby reducing the leakage current of the OSCs. Fig. 2c shows the high-resolution transmission electron microscopy (HTEM) of 2D GeSe. The lattice fringes of 2D GeSe can be clearly observed. The lattice fringes of the [011] crystal plane are the most obvious, and the corresponding interplanar spacing is 0.292 nm. Meanwhile, atomic force microscopy (AFM) is used to measure the thickness of 2D GeSe (Fig. 2d), and it is determined that 2D GeSe has an average thickness of about

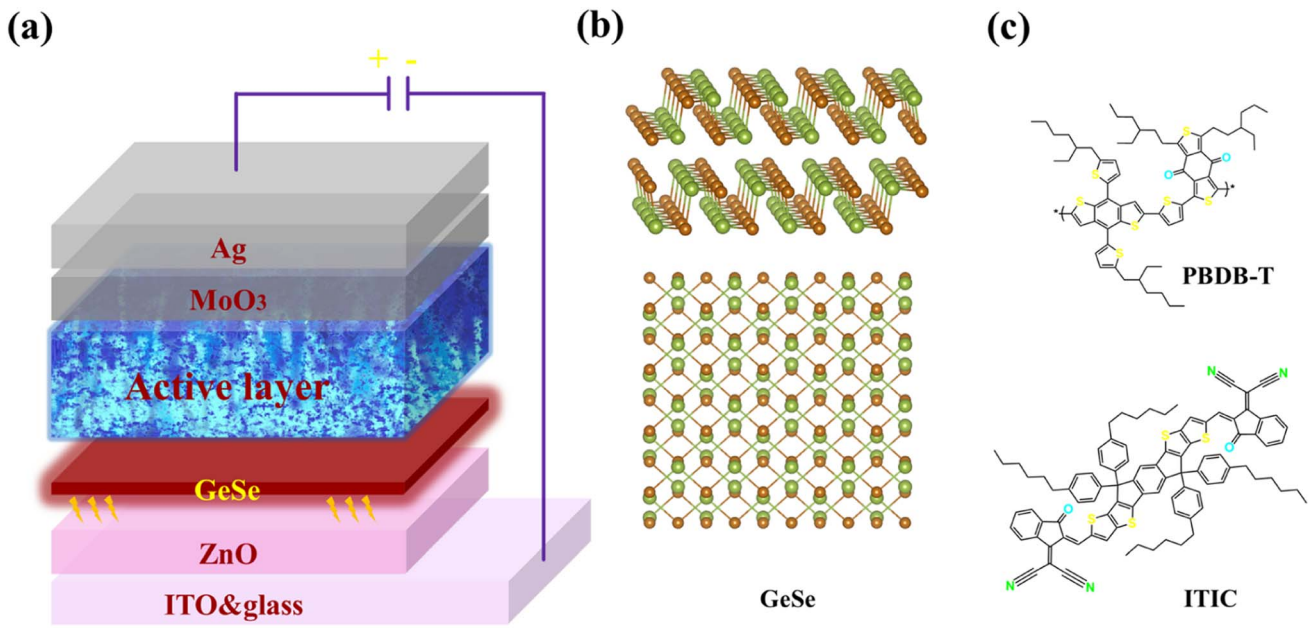

Fig. 1 (a) Structure diagram of the OSCs. (b) Structures of 2D GeSe (side view and top view). (c) Structures of PBDB-T and ITIC.

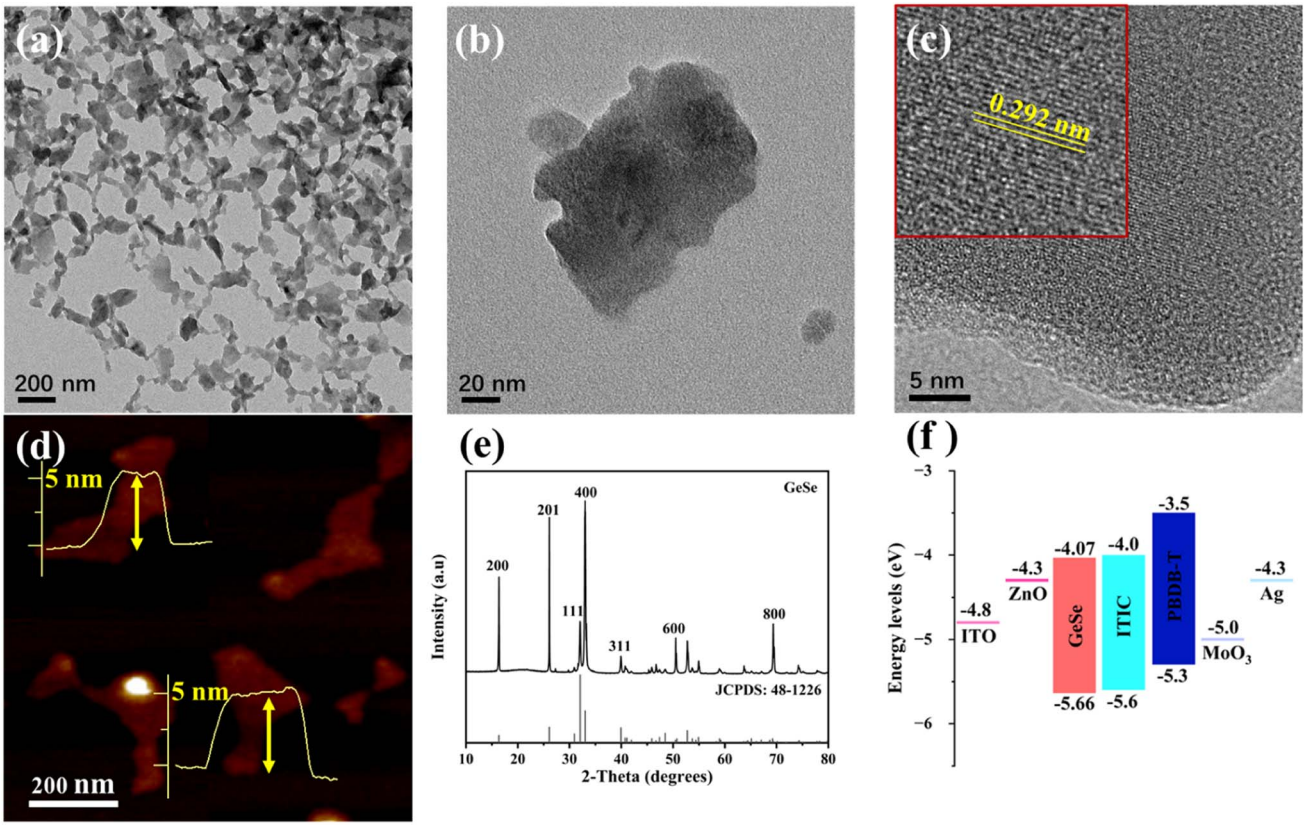

Fig. 2 (a and b) TEM images of 2D GeSe nanosheets. (c) HR-TEM image of 2D GeSe. (d) AFM image of 2D GeSe. (e) XRD pattern of GeSe. (f) The energy level diagram of OSCs.

5 nm. Previous studies have shown that the theoretical calculated thickness of monolayer GeSe is between 1 and 1.5 nm,[22] so it can be concluded that the nanosheets in the supernatant after centrifugation are few-layered (4–5 layers) nanosheets. X-ray diffraction (XRD) is used to verify the crystal structure of GeSe used in the experiment. As shown in Fig. 2e, each diffraction peak can correspond well to the XRD card (JCPDS: 48-1226). The energy of the conduction band (E_C) and valence band (E_V) of 2D GeSe is obtained by using the equations: $E_C = -4.71 - E_{ed}$ and $E_V = -4.71 - E_{ox}$, where E_{ed} and E_{ox} are measured by cyclic voltammetry (CV) (Fig. S1†) with a value of −0.64 and 0.95 eV. The energy level diagram of the device is shown in Fig. 2f. The stepped energy level arrangement formed between ZnO, GeSe and active layer materials is advantageous for electron transport in the OSCs.[23]

Calculation details

We use the first-principles Vienna *ab initio* software package (VASP) to calculate charge distribution and the coulomb interaction between ZnO and GeSe, in order to explore the electron transmission at the junction of ZnO and GeSe.[24] The generalized gradient approximation (GGA) of the Perdew–Burke–Ernzerhof (PBE) functional is used to describe the exchange of electrons and correlated interactions and the convergence test uses the plane-wave cutoff energy of 500 eV.[25,26] At the same time, the convergence criteria of energy are set to 1.0×10^{-5} eV, atoms are allowed to relax until the force on the atoms is less than 0.01 eV Å^{-1}, and the Monkhorst–Pack grid of $3 \times 3 \times 1$ was used for Brillouin region (BZ) integration.[27,28] Meanwhile, Grimme van der Waals (vdW) with zero-damping function (DFT-D3) is used to correct the potential energy with the dispersion interaction.[29] In order to avoid possible interactions between different supercells, 20 Å of vacuum space is set along the Z direction.

Geometric structure

We study the geometric structure of the ZnO crystal and double-layered GeSe before exploring the ZnO&GeSe composite ETL. For the ZnO crystal, the optimized lattice constants are $a = b =$ 3.27 Å with hexagonal wurtzite structure.[30] For double-layered GeSe, the calculated lattice constants are $a = 4.23$ Å and $b =$ 3.99 Å with orthogonal structure, which are consistent with the previous study.[31,32] In order to make the lattice constants of two different crystals match each other, ZnO and GeSe are expanded respectively. The base vectors a and b of the ZnO supercell are transformed to be mutually perpendicular by the translational symmetry of ZnO. The ZnO supercell has the calculated lattice constants of $a = 19.99$ Å, $b = 16.95$ Å and 2D GeSe has the calculated lattice constants of $a = 19.70$ Å and $b = 16.97$ Å. The lattice mismatches along the x and y directions are about 1.45% and 0.12% for the ZnO/GeSe composite. In addition, the ZnO/GeSe composite is constructed by stacking of four Zn–O

atomic layers and two layers of GeSe 2D material, and the whole model contains 144 Zn atoms, 144 O atoms, 80 Ge atoms and 80 Se atoms. All constructed supercells are the same size.

Coulomb interaction between the GeSe monolayer and ZnO crystal

The binding energy is defined as follows:

$$E_b = E_{GeSe+ZnO} - E_{GeSe} - E_{ZnO}$$

where $E_{GeSe+ZnO}$ is the total energy of the ZnO&GeSe composite ETL structure, E_{GeSe} is the energy of the GeSe monolayer and E_{ZnO} is the energy of the ZnO crystal.

In the ion-step self-consistent process, we fix the bottom two layers of Zn–O atoms in the model and relax all the atoms above them. The calculation results show that GeSe can stably combine with the Zn-face of ZnO. The average distance between the lower surface of 2D GeSe and the upper surface of ZnO is 2.8 Å, and the average binding energy between them is 62.1 meV $Å^{-2}$. This relatively high binding energy means that ZnO can firmly bind to 2D GeSe through van der Waals force, and the calculation model shows that this binding does not change the crystal structure of ZnO and GeSe (Fig. S2†). These results indicate that using GeSe as an interface modification material for ZnO does not destroy the crystal structure of ZnO and deteriorate the electrical properties of ZnO, which provides a prerequisite for GeSe to modify the surface of ZnO.

Furthermore, we calculate the differential charge density to explore the electron transport properties at the ZnO/GeSe interface; the 3D differential charge density is shown in Fig. 3a and b. When the surface of ZnO and GeSe is combined by van der Waals force, some electrons on the surface of GeSe will transfer to the ZnO/GeSe interface, which further proves the reason why the total energy of the system decreases when ZnO is combined with GeSe. In order to study the degree and direction of electron transfer more accurately, the *xz* plane section of the electron localization function (ELF) is shown in Fig. S3† and the planar averaged charge density difference of the ZnO/GeSe composite is shown in Fig. 3c. It can be seen that the electron density on the surface of GeSe decreases, which indicates that GeSe transfers electrons to the ZnO surface.

Previous studies have shown that if the surface charge of the ZnO crystal is not compensated, the net dipole moment diverges with increasing thickness, and the electrostatic potential monotonically increases, resulting in a very unstable polar surface of ZnO.[11] In general, the surface of ZnO will spontaneously produce many defects to offset the surface electric dipole moment, thereby reducing the surface energy and forming a relatively stable system.[12,13] In our calculation, the Zn–O atomic layer on the unmodified ZnO surface in the slab model of ZnO will shrink inward about 0.2 Å along the *z*-axis direction to balance the polarity of the surface, as shown in Fig. S2a† (in the real case, the polar surface is stabilized by spontaneously forming defects). However, after 2D GeSe modification, the surface Zn–O atomic layer distance of ZnO will be re-expanded along the *Z* axis by 0.09 Å, closer to the bulk structure of ZnO, as shown in Fig. S2b,† indicating that 2D GeSe can stabilize the surface of ZnO by compensating electrons, thereby improving the stability of the ZnO polar surface and reducing the formation of spontaneous defects.

GeSe transfers electrons to the ZnO surface, which will lead to the formation of the dipole moment at the ZnO/GeSe interface, and the direction of this dipole moment is ZnO pointing to GeSe, as shown in Fig. 3d. This interface electric dipole moment can promote the electron transfer from the GeSe interior to the GeSe surface, and then transfer to ZnO by quantum tunneling, thereby improving the electron transport efficiency. At the same time, there is also an electric dipole moment pointing to the direction of the active layer at the interface between GeSe and the active layer. Therefore, the electric dipole moment at the interface of the GeSe/active layer will promote GeSe to effectively extract electrons from the active layer and surface acceptor molecules. And the superimposed total electric dipole field will effectively promote the transfer of electrons from the active layer over 2D GeSe to the ZnO crystal, thereby improving the overall electrical performance of the OSCs.

In order to explore the reliability of theoretical calculation results from experiments, we use X-ray photoelectron spectroscopy (XPS) to detect the binding energy of the inner shell electrons of Zn and Ge atoms, and explore the change of the binding energy of each atom after modifying the ZnO crystal with 2D GeSe. The binding energy of the inner shell electrons of different atoms has its own characteristic energy, so XPS is often used to identify the elemental composition of the sample. At the same time, the binding energy of the inner shell electrons of the atom will also be affected by the environment around the atom. The full XPS spectrum of GeSe is shown in Fig. S4,† and the photoelectron peaks of Ge 3d and Se 3d can be clearly detected. They are located around 30 eV and 54 eV respectively, which are in good agreement with the expected binding energy. This proves that the material contains Ge and Se elements and is in the expected valence state of Ge^{2+} and Se^{2-}. The fine spectrum of Ge 3d is shown in Fig. 3e. When GeSe is used as an interface material to modify the ZnO crystal, the electron binding energy of Ge 3d increases from 29.70 eV to 30.08 eV. The increase of binding energy proves that the interaction between GeSe and ZnO reduces the electron density of Ge atoms. The fine spectrum of Zn 2P is shown in Fig. 3f. The photoelectron peaks of Zn $2P_{1/2}$ and Zn $2P_{1/2}$ are located at 1022.38 eV and 1045.46 eV respectively, which proves that Zn is in the valence state of +2. When ZnO is modified by GeSe, the photoelectron peaks of Zn $2P_{1/2}$ and Zn $2P_{1/2}$ move to 1021.76 eV and 1044.84 eV, respectively. The decrease of Zn 2p electron binding energy indicates that the interaction between GeSe and ZnO increases the electron density of Zn atoms. The change of XPS pattern demonstrates that there is electron transfer from Ge to Zn, which will lead to the formation of electric dipole moment pointing to GeSe at the interface between ZnO and GeSe. These results under macro-scale measurement are consistent with the conclusions obtained by first-principles calculations, which further proves the rationality of the inference. At the same time, we use the Kelvin probe to measure the work function (WF) of ZnO before and after modification. As shown in Fig. S5,† the WF of ZnO decreases from 4.35 eV to 4.18 eV after GeSe (the WF is

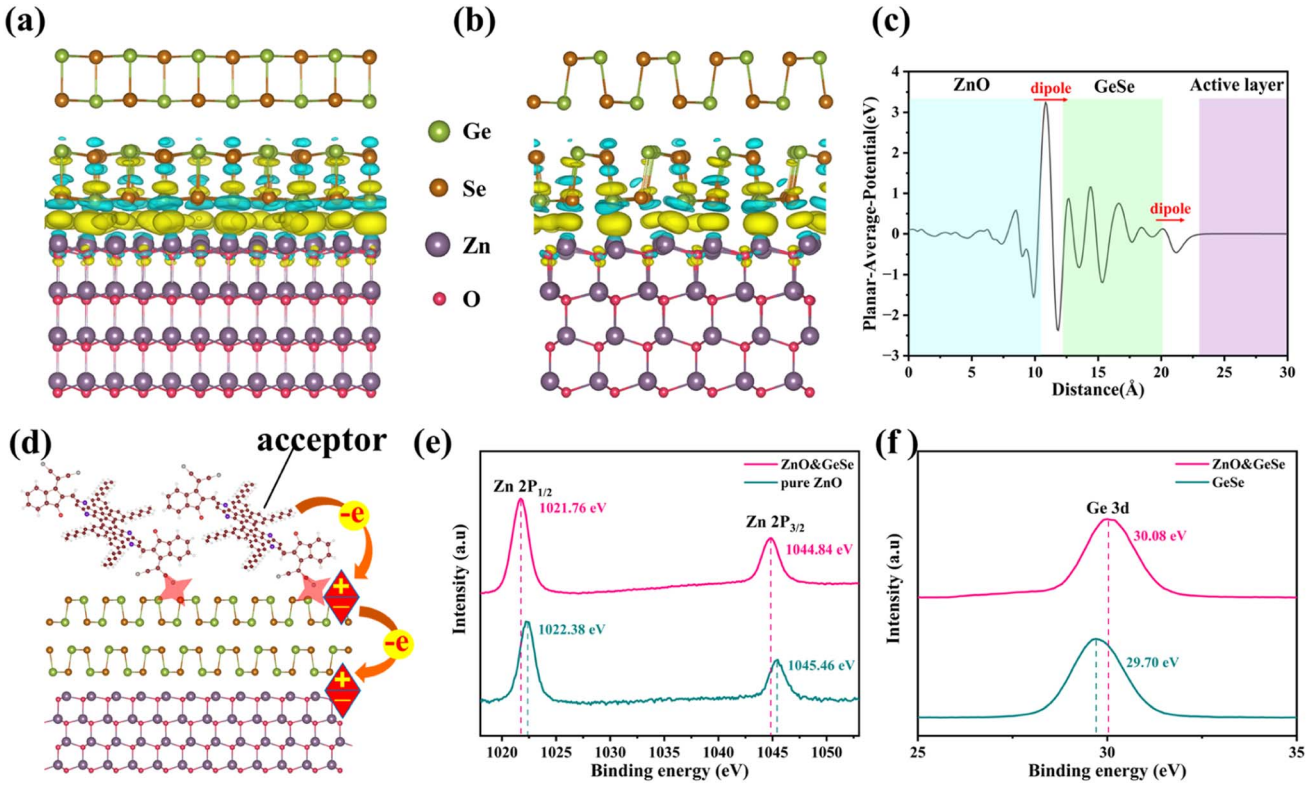

Fig. 3 (a) 3D differential charge density of the ZnO&GeSe composite ETL (iso-surface level is 0.002 electrons Å^{-3}) along the *x* direction and (b) *y* direction (the yellow and cyan iso-surfaces in the charge density difference figure represent the accumulation and depletion of electrons, respectively). (c) The integral curve of the difference charge density along the *z* direction. (d) A schematic diagram of the interface dipole moment and the charge transfer between the active layer, GeSe and ZnO. (e) XPS spectra of Zn 2p and (f) Ge 3d.

4.72 eV) modification, indicating that the electron concentration of ZnO increases and the energy required for electron overflow decreases, and the electric dipole moment from ZnO to GeSe is formed.

Modification of ZnO defect vacancies by GeSe

Since the surface of ZnO is a polar surface, it is easy to form point defect vacancies, which strongly affects the electron transport of ZnO. Therefore, in order to explore the effect of GeSe on the formation of ZnO defect vacancies, we calculated the formation energies of point defect vacancy, before and after covering 2D GeSe on the ZnO surface. The inhibition of 2D GeSe on the formation of ZnO vacancy defects is further investigated by comparing the defect formation energy before and after 2D modified by 2D GeSe. A previous study has shown that single Zn point defect vacancies are metastable on the surface, oxygen atoms near the single Zn atom point defect vacancy have a high probability of being captured by the surrounding Face Centered Cubic (FCC) sites and the electrostatic Madelung force drives to form bigger cavities on ZnO surfaces.[13] Therefore, we calculate two models of single Zn atom point vacancy defect and large cavity (three Zn atoms, one O atom), the schematic diagram of the defect vacancy is shown in Fig. 4a–c. 2D GeSe is superimposed on their surface and the total energy of the system is calculated. The difference of defect formation energy is defined as follows:

$$\Delta E = \left[\left(E_{\mathrm{ZnO(defect)+GeSe}} + E_{\mathrm{defect\ \ atom}}\right) + \sum_i n_i(\Delta\mu_i) + qE_{\mathrm{V}} - E_{\mathrm{ZnO+GeSe}}\right] - \left[\left(E_{\mathrm{ZnO(defect)}} + E_{\mathrm{defect\ \ atom}}\right) + \sum_i n_i(\Delta\mu_i) + qE_{\mathrm{V}} - E_{\mathrm{ZnO}}\right]$$

$E_{\mathrm{ZnO(defect)+GeSe}}$ is the total energy of ZnO (with defects) and GeSe. $E_{\mathrm{ZnO+GeSe}}$ is the total energy of ZnO (without defects) and GeSe. $E_{\mathrm{ZnO(defect)}}$ is the total energy of ZnO with defects. E_{ZnO} is the total energy of ZnO without defects. $\Delta\mu_i$ is the chemical potential of atoms and n_i is the number of missing atoms in the crystal when defects are formed. In our calculation, $\mu_{\mathrm{Zn}} + \mu_{\mathrm{O}} = -3.31$ eV, and we only discuss the case of electrical neutrality. Therefore, μ_{Zn} changes from 0 eV ($\mu_{\mathrm{O}} = -3.31$ eV) under Zn-rich (O-poor) conditions to -3.31 eV ($\mu_{\mathrm{O}} = 0$ eV) under Zn-poor (O-rich) conditions. The potential energy forming the defect is consistent with previous studies.[13]

The results show that the formation energy of Zn point defect vacancy (Fig. 4b) on the modified ZnO surface is 3.51 eV higher than that before modification, and the formation energy of large

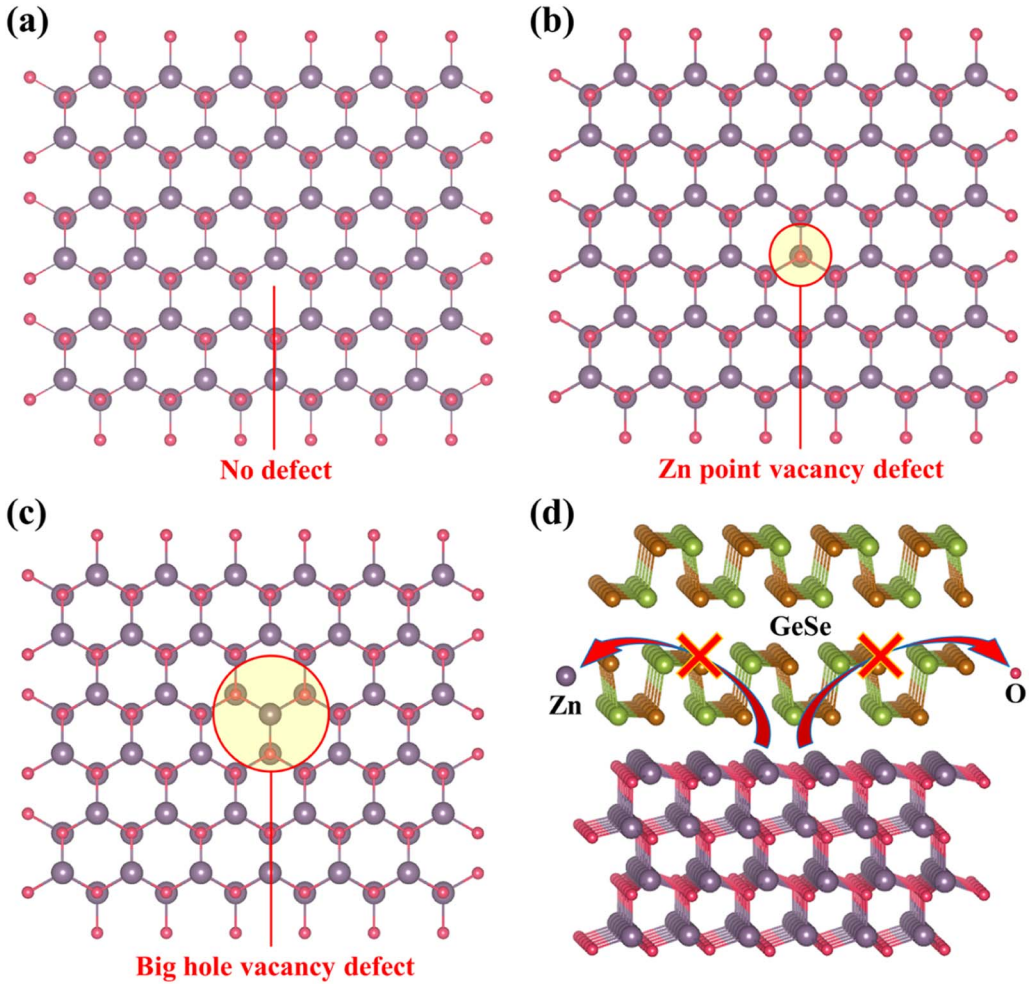

Fig. 4 (a) Unstable defect-free ZnO (0001) polar surface. (b) Zn point vacancy defect. (c) Big hole vacancy defect. (d) The schematic diagram of 2D GeSe inhibits the formation of ZnO defect vacancies.

cavity defect vacancy (Fig. 4c) on the modified ZnO surface is 5.83 eV higher than that before modification. The increase of defect formation energy indicates that it is more difficult to form defect vacancies on the surface of ZnO modified by 2D GeSe. The electrons transferring from GeSe to the ZnO surface offset the net dipole field established by the Zn–O ion plane, and the ZnO surface became more stable, so the formation of spontaneous defects is suppressed (Fig. 4d). 2D GeSe effectively inhibits the formation of defect vacancies on the surface of ZnO, and fewer defect vacancies mean that ZnO can maintain complete crystal structure, thereby improving the electronic collection and transmission of ZnO.

Scanning electron microscopy (SEM) is used to study the surface morphology of ZnO crystals, as shown in Fig. 5a–e. For the pure ZnO crystal, massive slits can be observed from the SEM image, and the existence of these slits greatly affects the electron collection and transmission at the interface. After using 2D GeSe to modify the surface of the ZnO crystal, we notice that most of the slits are filled by GeSe nanosheets, and the surface of the ZnO crystal becomes smoother. Some larger GeSe nanosheets appear on the surface of ZnO crystals. Among them, the GeSe nanosheets spin-coated at 2000 rpm and 1000 rpm on the surface of the ZnO crystal are the most obvious, and the low-speed spin-coating leads to a high content of GeSe nanosheets on the surface of ZnO. The 2D GeSe effectively repairs the gap between the nanocrystals on the ZnO surface, which will greatly enhance the ability of ZnO to collect and transport electrons from the active layer. In order to explore the effect of 2D GeSe on the crystallinity of ZnO, we measure the X-ray diffraction (XRD) spectra of ZnO before and after GeSe modification. As shown in Fig. 5f, after the modification of ZnO by 2D GeSe, each diffraction peak has increased significantly, and the diffraction peaks become sharper, which indicates that the crystallinity of ZnO has been significantly improved. Since 2D GeSe is spin-coated on the surface of the ZnO crystal, a small portion of the ZnO surface will dissolve and recrystallize during the second annealing process. At this time, GeSe inhibits the formation of defect vacancies on the surface of ZnO, and the smaller GeSe nanosheets fill the gap between ZnO grains, thus making ZnO crystals have better crystal quality.

The photoluminescence (PL) spectra are shown in Fig. 5g. The peak at 400 nm is the main emission peak, which is mainly

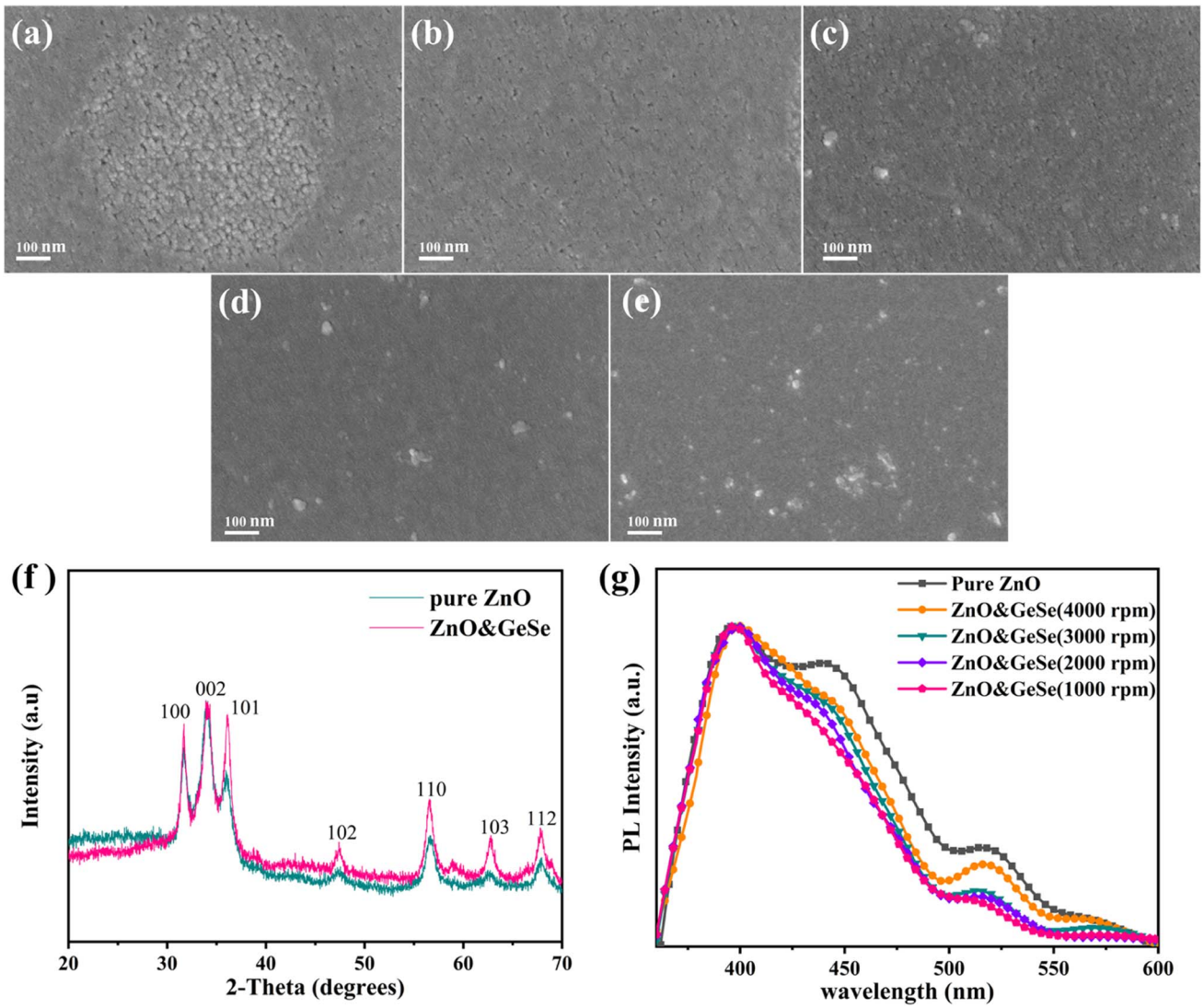

Fig. 5 SEM images of (a) pure ZnO ETL and ZnO covered by GeSe with the spin coating speeds of (b) 4000 rpm, (c) 3000 rpm, (d) 2000 rpm and (e) 1000 rpm. (f) XRD patterns of ZnO and ZnO&GeSe (2000 rpm). (g) Photoluminescence spectra of ZnO.

derived from the intrinsic exciton recombination of ZnO. The fluorescence intensity of the 400 nm emission peak is positively correlated with the crystal quality of the ZnO. The improvement of ZnO crystal quality is beneficial to promote exciton separation and electron transport. The other two emission peaks near 440 nm and 520 nm in the blue region are caused by defects in the ZnO crystal. The defects in the ZnO crystal cause a deep defect level, and the electrons excited to the defect level transitioning back to the valence band will emit blue-green fluorescence with a longer wavelength.[33] We notice that the intensity of the emission peaks of the defect energy level near 440 nm and 520 nm of the ZnO&GeSe ETL is smaller than that of the pure ZnO ETL. The ratio of the defect emission peak intensity to the intrinsic emission peak intensity of the ZnO&GeSe ETL is reduced from 0.877 (pure ZnO ETL) to 0.667 when the spin coating speed of 2D GeSe is 2000 rpm. Fig. S6† shows an in-depth XPS analysis of the O1s peak. For ZnO, the O1s region presents four main peaks at 530.1, 530.6, 531.0 and 531.5 eV, which correspond to lattice oxygen, defective oxygen, adsorbed oxygen and Zn–OH, respectively.[34,35] For ZnO/GeSe, the O1s peaks blue-shift to 529.6, 530.1, 530.6 and 531.2 eV, which further shows that ZnO obtains electrons after GeSe modification. Moreover, compared with ZnO films, the ratio of lattice oxygen to defect oxygen of ZnO/GeSe films increases from 0.66 to 0.92 (Table S1†). This indicates that the oxygen vacancy of ZnO decreases after GeSe modification. So the ZnO modified by 2D GeSe has higher crystal structure quality and fewer defects than pure ZnO, which helps to improve the performance of the ETL and reduces trap-assisted recombination at the ETL interface, and also enhances the stability of OSCs.

Optimization of vertical distribution in the active layer

In order to study the compatibility of the ZnO&GeSe composite ETL with the active layer material, we measure the water contact angles (WCAs) of the pure ZnO film and the ZnO&GeSe film

surface. As shown in Fig. 6a and b, the presence of 2D GeSe on the surface increases the WCA of the ETL from 51.7° for pure ZnO to 77.2° for ZnO/GeSe. The surface of ZnO is polar and more hydrophilic, but the surface of the 2D GeSe is saturated and more hydrophobic, and as shown in Fig. S7,† the WCA of the GeSe surface reaches 80.9°. The active layer material is hydrophobic; the more hydrophobic the surface of the ETL, the more favorable the compatibility between the ETL and the active layer molecules, thereby improving the crystallinity of the donor and acceptor molecules during the film formation of the active layer. At the same time, in order to investigate the effect of ZnO&GeSe on the vertical distribution of active layer components, we measure the WCAs of PBDB-T:ITIC active layers prepared on different ETLs, as shown in Fig. 6c and d. Among them, the WCA of the active layer prepared on the pure ZnO ETL is 101.3°, while the WCA of the active layer prepared on the ZnO&GeSe ETL is 104.2°. PBDB-T as a donor organic molecule is more hydrophobic and the ITIC molecule is less hydrophobic (Fig. S8†); the increase of WCA on the upper surface of the active layer means that 2D GeSe decreases the enrichment of acceptor molecules on the upper surface of the active layer; the diagram is shown in Fig. 6e. This is because the Ge atoms and Se point vacancy defects on the surface of GeSe have strong coulomb interaction with non-fullerene acceptor molecules (*e.g.* ITIC), so that acceptor molecules are adsorbed on the surface of GeSe, which promotes the vertical phase separation of the active layer donor and acceptor molecules.[36] Previous studies have also shown that 2D GeSe can improve the crystallinity and molecular orientation of the acceptor molecules, causing the acceptor molecules to aggregate on the surface of 2D GeSe in a π–π stacking manner. In organic photovoltaic devices, the improvement of AFM roughness on the surface of the active layer is a clear manifestation of the increase of the crystallinity of the active layer.[37,38] The AFM surface pattern of the active layer further demonstrates that the addition of GeSe improves the crystallinity of the active layer (Fig. S9†). The root mean square (RMS) of PDBD-T:ITIC with ZnO as ETL is 2.99 nm, while that of PDBD-T:ITIC with ZnO/GeSe as ETL is 4.56 nm. The results show that GeSe is conducive to the crystallization of the active layer. The improvement of crystallinity of the active layer and appropriate vertical phase separation can promote the transfer and collection of electrons and holes, which is beneficial to device stability and the improvement of OSC performance.

Performance characterization of OSCs

The performance parameters of PBDB-T:ITIC based OSCs with different types of ETLs are shown in Table 1. The J_{sc}, FF and V_{oc} of the control device with a pure ZnO crystal as ETL are 16.35 mA cm^{-2}, 67.15% and 0.917 V respectively, and the PCE of the device is 10.06%. At the same time, the PCE of the OSCs with ZnO&GeSe as ETL has significantly improved. When the spin coating speed is 2000 rpm, the PCE of OSCs with ZnO&GeSe as the ETL is the highest, and its PCE reaches 11.68%, which is about 16% higher than that of the blank control group, J_{sc} increases to 17.93 mA cm^{-2}, and FF increases to 70.23%, which can be attributed to the reduction of ZnO vacancy defects in ZnO&GeSe composite ETL, and the decrease of the recombination probability in OSCs. We notice that the PCE improvement of the ZnO&GeSe ETL device at low spin-coating speed (1000 rpm) is not as good as that at medium spin-coating speed (2000 rpm). This is because the GeSe film formed at low speed is too thick, and the transmission distance of electrons in GeSe is too long, which leads to the increase of carrier recombination probability. Compared with the device with pure ZnO ETL, the V_{oc} of the ZnO&GeSe device is slightly improved, which may be caused by the photovoltage generated by the van der Waals heterojunction formed between ZnO and GeSe. The *J*–*V* curve of the device under simulated sunlight is shown in Fig. 7a, and the

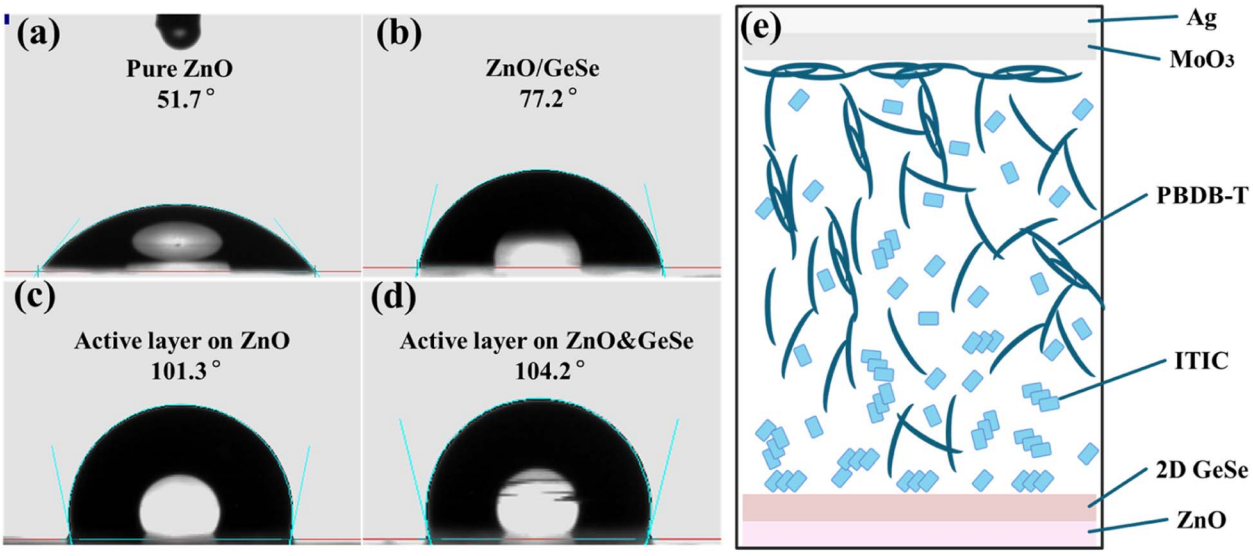

Fig. 6 Water contact angles on the surface of (a) pure ZnO, (b) ZnO&GeSe ETL, (c) PBDB-T:ITIC with ZnO ETL and (d) PBDB-T:ITIC on ZnO&GeSe composite ETL (2000 rpm). (e) Diagram of the distribution change of each component in the active layer at the vertical direction.

Table 1 Parameters of OSCs with different ETLs[a]

Type	ETL	J_{sc} (mA cm^{-2})	Cal. J_{sc} (mA cm^{-2})	V_{oc} (V)	FF (%)	PCE (%)
PBDB-T:ITIC	ZnO	16.35 ± 0.08	15.68	0.917 ± 0.010	67.15 ± 0.42	10.06 ± 0.10
	ZnO/GeSe (4000 rpm)	16.68 ± 0.09	16.01	0.920 ± 0.011	68.76 ± 0.56	10.55 ± 0.11
	ZnO/GeSe (3000 rpm)	17.05 ± 0.13	16.39	0.922 ± 0.013	68.94 ± 0.68	10.84 ± 0.14
	ZnO/GeSe (2000 rpm)	17.93 ± 0.16	17.36	0.928 ± 0.013	70.23 ± 0.71	11.68 ± 0.17
	ZnO/GeSe (1000 rpm)	17.69 ± 0.15	17.06	0.931 ± 0.014	68.89 ± 0.60	11.35 ± 0.16
PM6:Y6	ZnO	25.43 ± 0.17	24.74	0.838 ± 0.009	71.33 ± 0.72	15.20 ± 0.18
	ZnO/GeSe (2000 rpm)	27.02 ± 0.19	26.33	0.843 ± 0.009	76.87 ± 0.74	17.51 ± 0.20

[a] Average J_{sc}, V_{oc}, FF and PCE of 30 devices.

corresponding *J–V* curve under darkness is shown in Fig. 7b. According to the change of dark conduction *J–V* curve, we find that the leakage current of the device with ZnO&GeSe as ETL is reduced, and the whole device has a higher rectification ratio and better diode characteristics. At the same time, the external quantum efficiency (EQE) of different ETL devices is shown in Fig. 7c. We find that the values of EQE increase significantly. The calculated J_{sc} values obtained by integrating the EQE curve match well with the J_{sc} values obtained by *J–V* currents.

In order to further understand the influence of different ETLs on the overall conductivity of the device, we measure the electrochemical impedance spectroscopy (EIS) of different devices under lightless conditions, and the fitted Nyquist diagram and the equivalent circuit diagram are shown in Fig. S10.† The related fitting parameters are shown in Table S2,† where R_S and R_Q represent the ohmic components of series resistance and bulk resistance, respectively. We find that the R_S and R_Q of OSCs with the ETL of ZnO&GeSe are lower than those with the ETL of pure ZnO. In particular, the device with the ETL of ZnO&GeSe (2000 rpm) has the lowest values of R_S and R_Q, which are 15.1 Ω and 4.04 kΩ respectively, which proves that 2D GeSe modified ZnO can reduce the impedance of the device, improve the carrier mobility at the interface and the active layer, and make the device have better conductivity.

Fig. 7d shows the stability of the pure ZnO ETL device and ZnO&GeSe ETL device. The device is not packaged, stored in a dark, nitrogen-filled glove box, and removed from the glove box after each period of time and measured under simulated sunlight. Compared with pure ZnO ETL OSCs, the PCE decay of the OSCs using ZnO&GeSe as ETL is significantly suppressed,

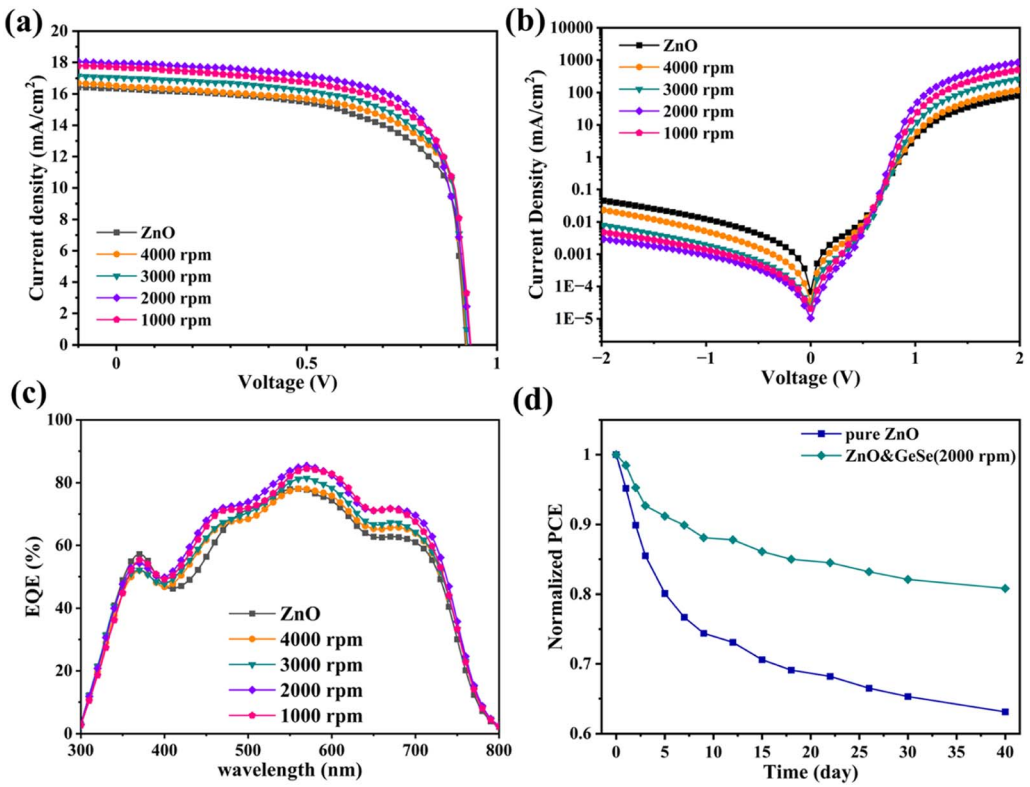

Fig. 7 (a) *J–V* curves of OSCs based on PBDB-T:ITIC with ZnO ETL and ZnO&GeSe composite ETL. (b) Corresponding dark conduction curves. (c) Corresponding EQE spectra. (d) The stability of OSCs with ZnO ETL and ZnO&GeSe composite ETL.

which indicates that the stability of the device has been greatly improved by using the 2D GeSe interface layer. Previous studies have reported that ZnO has photocatalytic activity under ultraviolet light irradiation, which will decompose the non-fullerene acceptors in the active layer, increase carrier recombination loss and result in poor stability of OSCs.[39] The 2D GeSe located between ZnO and the active layer can act as a shield, effectively preventing the decomposition of non-fullerene acceptors in the active layer by ZnO. The improvement of the crystallinity of the acceptor molecules also enhances the stability of OSCs.[36] Meanwhile, GeSe has oxidation resistance, preventing water and oxygen from invading ZnO, and the binding of 2D GeSe to ZnO surface atoms also reduces the probability of ZnO forming vacancy defects and improves the stability of ZnO crystals. The improvement of the crystalline quality of ZnO greatly enhances the stability of OSCs.

We also study the versatility of the ZnO&GeSe composite ETL in OSCs of other active layer materials. When ZnO&GeSe composite ETL is used in OSCs with PM6 as donor and Y6 as acceptor (the device structure is ITO/ETL/PM6:Y6/MoO_3/Ag), the PCE of the device increases from 15.20% for the control group (pure ZnO as ETL) to 17.51%, the J_{sc} increases from 25.43 mA cm^{-2} to 27.02 mA cm^{-2}, the V_{oc} increases from 0.838 V to 0.843 V, and the FF increases from 71.33% to 76.87%; the J–V curve is shown in Fig. S11a.† The corresponding J–V curve under darkness is shown in Fig. S11b,† indicating that in the PM6:Y6 system, the OSCs with the ZnO&GeSe ETL has better diode characteristics. The EQE of the device based on PM6:Y6 with ETL of ZnO&GeSe is also higher than the control group, as shown in Fig. S11c.† The integral current increased from 24.74 mA cm^{-2} in the control group to 26.33 mA cm^{-2}, which corresponds to the short-circuit current in the J–V curve. The reason why ZnO&GeSe is still applicable in the PM6:Y6 system and improves the device performance is mainly due to the similarity of the structure and functional groups of the acceptor molecules ITIC and Y6. They have similar molecular structures and contain two cyano groups at both ends of the molecule. The cyano group is the key to the coulomb interaction between these two acceptor molecules and 2D GeSe, and the acceptor molecules are enriched on the surface of GeSe, thereby improving the vertical distribution of the active layer, improving the carrier transport and collection efficiency, and ultimately increasing the PCE of OSCs.

We use the J_{sc}–intensity dependence curve to explore the change of carrier recombination process in OSCs before and after 2D GeSe modification. The relationship between J_{sc} and light intensity can be expressed by the formula $J_{sc} \propto I^{\alpha}$.[40] The closer the value of α tends to 1, the more likely the bimolecular recombination probability of OSCs tends to be 0. The fitted J_{sc}–light intensity dependence curve is shown in Fig. 8a. The α value of the J_{sc}–light intensity dependence curve is increased from 0.930 for the OSCs with pure ZnO as ETL to 0.979 for the OSCs with ZnO&GeSe as ETL, indicating that the ZnO&GeSe composite ETL can inhibit the bimolecular recombination in OSCs, which is beneficial to the improvement of the fill factor of OSCs. We also studied the effect of the ZnO&GeSe ETL on trap-assisted carrier recombination in OSCs by measuring the V_{oc}–intensity dependence curve. As shown in Fig. 8b, the relationship between V_{oc} and light intensity can be expressed by the natural logarithm formula $V_{oc} \propto n\frac{kT}{e}\ln(I)$,[41] where k is the Boltzmann constant, T represents the absolute temperature, and e represents the charge of a single electron. The slope of the fitting curve in the logarithmic coordinate is related to the type of carrier recombination in the device. The slope of 1 kT/e indicates that the device is dominated by carrier bimolecular recombination, and the slope of 2 kT/e indicates that the device is dominated by trap-assisted recombination. The values of n of the fitted curves are 1.3, 1.22, 1.14, 1.05 and 1.15 respectively, indicating that the ZnO&GeSe composite ETL can effectively reduce the trap-assisted recombination in the device, thereby improving the collection efficiency of free carriers. This is mainly due to the reduction of defect vacancies in ZnO crystals and the better crystal morphology formed on the ZnO surface, which is conducive to the further improvement of the FF.

To further analyze exciton generation, dissociation, and collection efficiency in the OSCs with the ZnO&GeSe composite ETL, we measure the relationship between photocurrent density (J_{ph}) and effective voltage (V_{eff}), as shown in Fig. 8c. The photoelectricity at the maximum output power is counted. The photocurrent density at maximum output power (J_{mp}) and saturated photocurrent density (J_{sat}) are listed in Table 2. The exciton dissociation probability can be calculated by the formula $P_{diss} = J_{sc}/J_{sat}$, and the charge collection efficiency can be obtained by the formula $P_{coll} = J_{mp}/J_{sat}$. We find that P_{diss} in ZnO&GeSe composite ETL devices is significantly improved compared with pure ZnO ETL devices. P_{diss} increases from 87.99% (pure ZnO) to 92.28% (ZnO&GeSe 2000 rpm) exciton dissociation efficiency, indicating that devices with ZnO&GeSe as ETL are more conducive to exciton dissociation, which is closely related to the optimization of the vertical morphology of the active layer. As the substrate of the active layer, the GeSe layer effectively promotes the π–π stacking of acceptor molecules on the surface of GeSe (the bottom of the active layer) to form a continuous conductive network. The P_{coll} increases from 67.38% for the device with pure ZnO as ETL to 77.24% for the ZnO&GeSe composite ETL device (ZnO&GeSe 2000 rpm), indicating that GeSe as the interface layer greatly improves the charge collection efficiency of OSCs, which is mainly due to the better electron collection and transmission ability of the ZnO&GeSe composite ETL. Meanwhile, the enrichment of receptor molecules on the surface of GeSe is also beneficial to the collection of electrons on the surface of the ETL. However, when the thickness of the GeSe layer is too large (1000 rpm), it is not conducive to the further improvement of exciton dissociation efficiency and charge collection efficiency. The reason may be that the over-thickness of the GeSe layer leads to the excessive aggregation of acceptor molecules on the surface of GeSe, which reduces the contact area between donor molecules and acceptor molecules in the active layer, resulting in the decrease of exciton dissociation efficiency. The over-thickness of the ETL also hinders the transmission of photogenerated electrons, resulting in the decrease of charge collection efficiency. The maximum exciton generation rate (G_{max}) of OSCs can be

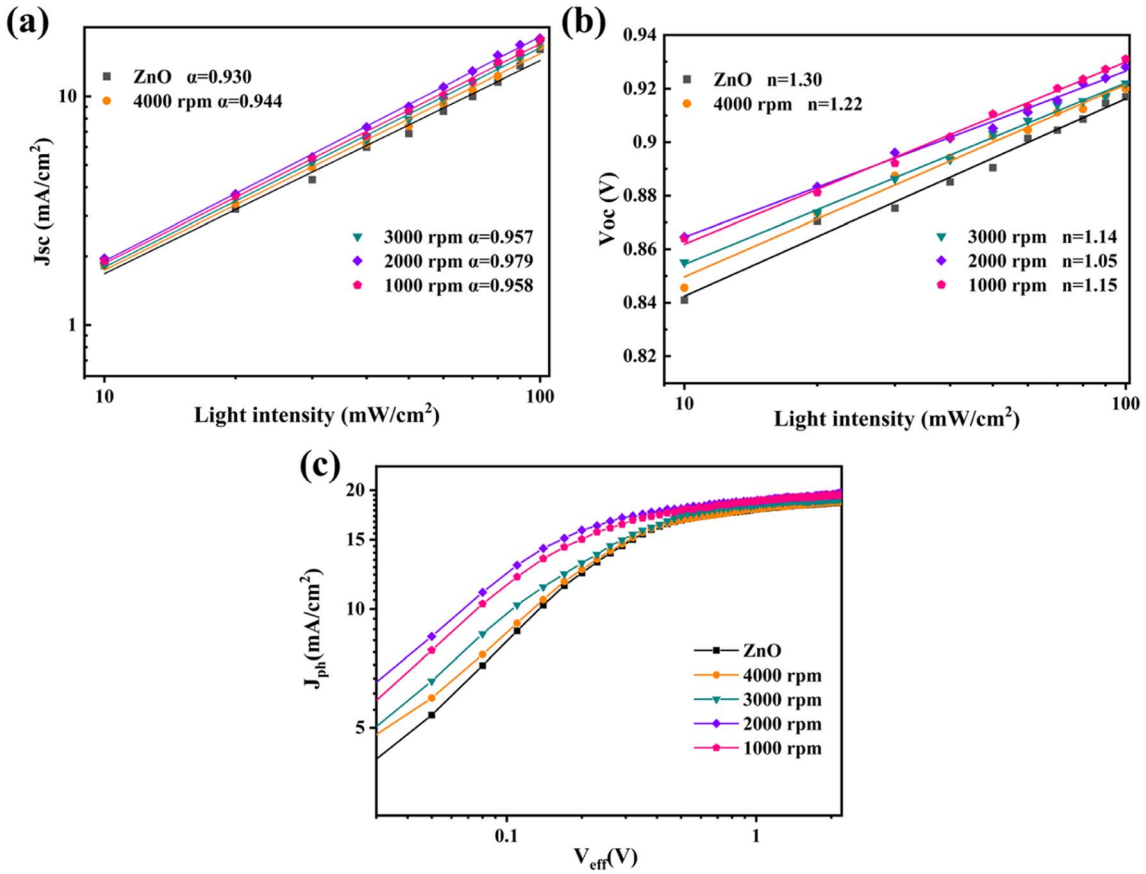

Fig. 8 (a) J_{sc}–light, (b) V_{oc}–light and (c) J_{ph}–V_{eff} intensity curves of OSCs with different types of ETL.

Table 2 Summary of the J_{sat}, P_{coll}, P_{diss}, and G_{max} values of OSCs

Type	ETL	J_{mp} (mA cm^{-2})	J_{sat} (mA cm^{-2})	P_{coll} (%)	P_{diss} (%)	G_{max} ($\times 10^{28}$)
A	ZnO	12.522	18.581	67.38	87.99	1.160
B	ZnO&GeSe (4000 rpm)	13.738	18.721	73.38	89.11	1.169
C	ZnO&GeSe (3000 rpm)	14.052	18.755	74.92	89.98	1.171
D	ZnO&GeSe (2000 rpm)	15.007	19.427	77.24	92.28	1.213
E	ZnO&GeSe (1000 rpm)	14.573	19.547	74.55	90.50	1.220

calculated by the formula $G_{max} = J_{sat}/eL$. In the OSCs using the ZnO&GeSe composite ETL, the G_{max} increases from 1.160×10^{28} for the OSCs using pure ZnO as ETL to 1.220×10^{28} (ZnO&GeSe 1000 rpm), mainly due to the photoelectric effect of 2D GeSe itself. The energy level difference formed between GeSe and ZnO can also separate some photogenerated excitons, thereby increasing the overall exciton generation rate of OSCs.

Conclusion

In conclusion, we prepared a ZnO&GeSe composite and used it as the ETL of OSCs for the first time. The PCE of OSCs based on PBDB-T:ITIC and PM6:Y6 increases from 10.06% and 15.20% to 11.68% and 17.51%, respectively. Our first-principles calculations show that electrons accumulated at the interface between ZnO and GeSe models. The transfer of electrons from GeSe to the surface of ZnO can not only offset the net dipole field accumulated along the z direction established by the oppositely charged atomic layers of Zn and O on the ZnO surface, which stabilizes the polar surface of ZnO and reduces the formation of spontaneous defects on the polar surface of ZnO, as well as bringing the ZnO surface closer to the bulk phase, but can also form new interface electric dipole moments to promote the transmission and collection of electrons. Meanwhile, the calculations also show that the formation energy of point vacancy defects on the surface of ZnO increases after GeSe modification, indicating that GeSe does effectively inhibit the formation of ZnO vacancy defects. Meanwhile, the experimental characterizations show that some electrons in GeSe are transferred to ZnO crystals, and the defect density of ZnO crystals also decreases, which proves the reliability of the theoretical research conclusions, and shows the application potential of 2D

GeSe as an interface transport layer, which provides research ideas for 2D materials to modify the defects of ZnO and other crystals.

Experimental process and fabrication details

The relevant experimental steps are described in detail in the auxiliary data, including the source of raw materials used in the experiment, the preparation and characterization of 2D GeSe, the preparation methods of the ZnO&GeSe ETL and OSCs, and the experimental characterization methods of the ETL.

Conflicts of interest

The authors declare no conflict of interest.

Acknowledgements

This work was financially supported by the National Natural Science Foundation of China (No. 61974045) and the Natural Science Foundation of Guangdong Province (No. 2023A1515012733, 2019A1515012092).

References

1 Y. Lin, J. Wang, Z.-G. Zhang, H. Bai, Y. Li, D. Zhu and X. Zhan, *Adv. Mater.*, 2015, **27**, 1170–1174.
2 J. Yuan, Y. Zhang, L. Zhou, G. Zhang, H.-L. Yip, T.-K. Lau, X. Lu, C. Zhu, H. Peng, P. A. Johnson, M. Leclerc, Y. Cao, J. Ulanski, Y. Li and Y. Zou, *Joule*, 2019, **3**, 1140–1151.
3 M. Zhang, X. Guo, W. Ma, H. Ade and J. Hou, *Adv. Mater.*, 2015, **27**, 4655–4660.
4 C. Q. Li, X. Zhang, N. Yu, X. B. Gu, L. Q. Qin, Y. A. Wei, X. Z. Liu, J. Q. Zhang, Z. X. Wei, Z. Tang, Q. Q. Shi and H. Huang, *Adv. Funct. Mater.*, 2022, **32**, 2108861.
5 S. Fang, J. Huang, R. Tao, Q. Wei, X. Ding, S. Yajima, Z. Chen, W. Zhu, C. Liu, Y. Li, N. Yin, L. Song, Y. Liu, G. Shi, H. Wu, Y. Gao, X. Wen, Q. Chen, Q. Shen, Y. Li, Z. Liu, Y. Li and W. Ma, *Adv. Mater.*, 2023, **21**, 2212184.
6 L. Zhu, M. Zhang, J. Xu, C. Li, J. Yan, G. Zhou, W. Zhong, T. Hao, J. Song, X. Xue, Z. Zhou, R. Zeng, H. Zhu, C.-C. Chen, R. C. I. MacKenzie, Y. Zou, J. Nelson, Y. Zhang, Y. Sun and F. Liu, *Nat. Mater.*, 2022, **21**, 656–663.
7 Q. P. Fan, R. J. Ma, J. Yang, J. S. Gao, H. R. Bai, W. Y. Su, Z. Z. Liang, Y. Wu, L. X. Tang, Y. X. Li, Q. Wu, K. Wang, L. H. Yan, R. Zhang, F. Gao, G. Li and W. Ma, *Angew. Chem., Int. Ed.*, 2023, **62**, e202308307.
8 F. Qin, W. Wang, L. Sun, X. Jiang, L. Hu, S. Xiong, T. Liu, X. Dong, J. Li, Y. Jiang, J. Hou, K. Fukuda, T. Someya and Y. Zhou, *Nat. Commun.*, 2020, **11**, 4508.
9 J. Huang, Z. Yin and Q. Zheng, *Energy Environ. Sci.*, 2011, **4**, 3861–3877.
10 S. Chen, C. E. Small, C. M. Amb, J. Subbiah, T. Lai, S.-W. Tsang, J. R. Manders, J. R. Reynolds and F. So, *Adv. Energy Mater.*, 2012, **2**, 1333–1337.
11 O. Dulub, U. Diebold and G. Kresse, *Phys. Rev. Lett.*, 2003, **90**, 016102.
12 H. Xu, L. Dong, X. Shi, Y. Liu, M. A. Van Hove, N. Lin and S. Y. Tong, *J. Phys. Chem. C*, 2016, **120**, 26915–26921.
13 H. Xu, L. Dong, X. Q. Shi, M. A. Van Hove, W. K. Ho, N. Lin, H. S. Wu and S. Y. Tong, *Phys. Rev. B: Condens. Matter Mater. Phys.*, 2014, **89**, 235403.
14 S. Lin, S. Liu, Z. Yang, Y. Li, T. W. Ng, Z. Xu, Q. Bao, J. Hao, C.-S. Lee, C. Surya, F. Yan and S. P. Lau, *Adv. Funct. Mater.*, 2016, **26**, 864–871.
15 F. Wang, Y. Zhang, M. Yang, J. Du, L. Xue, L. Yang, L. Fan, Y. Sui, J. Yang and X. Zhang, *Nano Energy*, 2019, **63**, 103825.
16 J. Chen, J. Zhang, C. Huang, Z. Bi, X. Xu and H. Yu, *Chem. Eng. J.*, 2021, **410**, 128436.
17 J. Choi, Y. Kim, J. W. Jo, J. Kim, B. Sun, G. Walters, F. P. García de Arquer, R. Quintero-Bermudez, Y. Li, C. S. Tan, L. N. Quan, A. P. T. Kam, S. Hoogland, Z. Lu, O. Voznyy and E. H. Sargent, *Adv. Mater.*, 2017, **29**, 1702350.
18 Z. Wang, Y. Ren, J. Meng, X. Zou, S. Wang, M. Zhao, H. Wang, Y. Hao, B. Xu, E. Wang and S. Yin, *J. Mater. Chem. A*, 2023, **11**, 1810–1816.
19 A. Onodera, I. Sakamoto, Y. Fujii, N. Mori and S. Sugai, *Phys. Rev. B: Condens. Matter Mater. Phys.*, 1997, **56**, 7935–7941.
20 P. D. Antunez, J. J. Buckley and R. L. Brutchey, *Nanoscale*, 2011, **3**, 2399–2411.
21 G. Shi and E. Kioupakis, *Nano Lett.*, 2015, **15**, 6926–6931.
22 H. Zhao, Y. Mao, X. Mao, X. Shi, C. Xu, C. Wang, S. Zhang and D. Zhou, *Adv. Funct. Mater.*, 2018, **28**, 1704855.
23 S. Li, L. Ye, W. Zhao, S. Zhang, S. Mukherjee, H. Ade and J. Hou, *Adv. Mater.*, 2016, **28**, 9423–9429.
24 G. Kresse and J. Hafner, *Phys. Rev. B: Condens. Matter Mater. Phys.*, 1993, **47**, 558–561.
25 J. P. Perdew, K. Burke and M. Ernzerhof, *Phys. Rev. Lett.*, 1997, **78**, 1396.
26 G. Kresse and D. Joubert, *Phys. Rev. B: Condens. Matter Mater. Phys.*, 1999, **59**, 1758–1775.
27 G. Kresse and J. Furthmüller, *Comput. Mater. Sci.*, 1996, **6**, 15–50.
28 H. J. Monkhorst and J. D. Pack, *Phys. Rev. B: Solid State*, 1976, **13**, 5188–5192.
29 S. Grimme, *J. Comput. Chem.*, 2006, **27**, 1787–1799.
30 C. G. Van de Walle, *Phys. Rev. Lett.*, 2000, **85**, 1012–1015.
31 D. J. Xue, S. C. Liu, C. M. Dai, S. Chen, C. He, L. Zhao, J. S. Hu and L. J. Wan, *J. Am. Chem. Soc.*, 2017, **139**, 958–965.
32 D. D. Vaughn, R. J. Patel, M. A. Hickner and R. E. Schaak, *J. Am. Chem. Soc.*, 2010, **132**, 15170–15172.
33 H. B. Zeng, G. T. Duan, Y. Li, S. K. Yang, X. X. Xu and W. P. Cai, *Adv. Funct. Mater.*, 2010, **20**, 561–572.
34 C. W. Huang, J. Y. Tian, S. Yang, Y. J. Zhao and H. Z. Yu, *Nano Energy*, 2023, **115**, 108691.
35 D. Zheng, G. Wang, W. Huang, B. Wang, W. Ke, J. L. Logsdon, H. Wang, Z. Wang, W. Zhu, J. Yu, M. R. Wasielewski, M. G. Kanatzidis, T. J. Marks and A. Facchetti, *Adv. Funct. Mater.*, 2019, **29**, 1900265.
36 J. Tan, Y. Zhao, G. Li, S. Yang, C. Huang and H. Yu, *Adv. Funct. Mater.*, 2022, **32**, 2209094.

37 J. B. Zhao, Y. K. Li, G. F. Yang, K. Jiang, H. R. Lin, H. Ade, W. Ma and H. Yan, *Nat. Energy*, 2016, **1**, 15027.
38 J. Min, Y. N. Luponosov, N. Gasparini, M. Richter, A. V. Bakirov, M. A. Shcherbina, S. N. Chvalun, L. Grodd, S. Grigorian, T. Ameri, S. A. Ponomarenko and C. J. Brabec, *Adv. Energy Mater.*, 2015, **5**, 1500386.
39 Y. Jiang, L. Sun, F. Jiang, C. Xie, L. Hu, X. Dong, F. Qin, T. Liu, L. Hu, X. Jiang and Y. Zhou, *Mater. Horiz.*, 2019, **6**, 1438–1443.
40 J. Zhang, B. Yu, Y. Sun and H. Yu, *Adv. Energy Mater.*, 2023, **13**, 2300382.
41 C. W. Huang and H. Z. Yu, *Nano Energy*, 2022, **103**, 107750.

